Academic Journal of Science and Technology
ISSN: 2771-3032 | Vol. 21, No. 1, 2026

First-principles and Experimental Study on Structure and Properties of Fe20Co20Cr20Ni25AlxTi(15-x) High Entropy Alloy Coatings

Xiong Yang*, Yarong Chen, Ruiwen Chen, Shixiang Cheng, Weihao Chen, Senpeng Fang, Yong Chen, Dan Huang, Xing Fang

Chengdu Aircraft Industrial (Group) Co., Ltd., Chengdu 610092, China.

* Corresponding author

Abstract: In this study, based on DFT-based first-principles calculations and the design philosophy of multi-component alloy segmented design, a high-entropy alloy system of Fe20Co20Cr20Ni25AlxTi(15-x) (x = 0, 5, 10, 15) was designed to investigate the synergistic effects of Al and Ti on phase stability, electronic properties, and elastic properties. The designed Fe20Co20Cr20Ni25AlxTi(15-x) high-entropy alloy exhibits good stability; there are no significant differences in the band density among the various high-entropy alloys, and all exhibit metallic properties. The addition of Al and Ti did not compromise the stability of the high-entropy alloy system. Under optimal conditions, defect-free, well-formed high-entropy alloy coatings were successfully prepared. Under optimal conditions, defect-free, well-formed high-entropy alloy coatings were successfully prepared. The basic mechanical properties of the high-entropy alloy coatings were investigated, resulting in a Fe20Co20Cr20Ni25Al5Ti10 high-entropy alloy coating with excellent mechanical properties.

Keywords: Laser cladding; Frist-principles; Micro-shearing; Tensile testing at room temperature.

1. Introduction

During the alloy design phase, it is necessary to select the appropriate elemental composition and corresponding preparation method for high-entropy alloys based on the material's operating environment. In recent years, multiscale computational and simulation methods based on materials science have developed rapidly and been widely applied in materials research, providing an efficient approach for the development of novel high-entropy alloys. First-principles calculations are a research method that aims to understand multi-atom systems by analyzing multi-particle systems composed of electrons and atomic nuclei, and to elucidate the structure and physical properties of materials by studying the motion of electrons. Research has found that commonly used computational methods currently include Density Functional Theory (DFT), Ab Initio Thermodynamics (AITD), Ab Initio Molecular Dynamics (AIMD), and the Calculation of Phase Diagrams (CALPHAD) method, among others.[1]. Density Functional Theory (DFT) is a quantum mechanical method for studying the electronic structure of many-electron systems; its central idea is to use electron density to describe many ground-state physical properties of atoms, molecules, and solids.

Research has shown that commonly used computational models for high-entropy alloy solid solutions currently include the simple supercell (SC), the virtual crystal approximation (VCA), the coherent potential approximation (CPA), and the special quasi-random structure (SQS) method[2]. VCA involves replacing actual alloy atoms with virtual atoms composed of the weighted average of the various alloying elements. This method preserves structural symmetry and requires minimal computational effort, but it does not account for factors such as lattice distortion and the local atomic environment. The CPA method is commonly used to address issues such as chemical and magnetic disorder in solid solutions; while it is computationally efficient, it is unable to account for lattice distortion. The SQS method models a supercell lattice structure in which alloying elements are randomly distributed across lattice sites, thereby yielding disordered structures with different atomic configurations. This modeling method accounts for the influence of the local atomic environment, ensuring computational accuracy and reliability. In summary, researchers have proposed and summarized a wide range of predictive methods to achieve precise control over phase stability in high-entropy alloys and to screen for phase formation through composition tuning. Currently, the focus of research has shifted from theoretical prediction to studies on the "structure–property" correlations of high-entropy alloys and investigations into microstructural deformation mechanisms.

The FeCoCrNi system was selected as the base system; the functions of the elements comprising the high-entropy alloy are shown in Table 1. The properties of Fe, Co, Cr, and Ni meet the requirements for a coating designed to achieve defect-free, high wear resistance, and excellent thermal fatigue performance, as outlined in this paper. Therefore, this study focuses on high-entropy FCC-FeCoCrNi alloys, which are characterized by good toughness but relatively low strength. In high-entropy alloys, the hysteretic diffusion effect influences atomic diffusion during solidification; the diffusion of large atoms may be impeded, leading to the precipitation of a second phase during solidification. The precipitation hardening effect of this second phase enhances the mechanical properties of the alloy. The addition of Al improves high-temperature oxidation resistance and wear resistance[3], The addition of titanium significantly increases the microhardness of the coating[4]. The simultaneous addition of Al and Ti, which have larger atomic sizes, promotes second-phase strengthening in high-entropy FeCoCrNi alloys. Furthermore, by adjusting the molar ratio of Al and Ti, the volume fraction of the second phase can be

controlled, thereby enabling the regulation of material properties[5]. For this purpose, high-entropy alloy powders were selected with the composition Fe20Co20Cr20Ni25AlxTi(15-x) (x = 0, 5, 10, 15), where x represents the atomic ratio of added aluminum. For the sake of brevity in the following description, the high-entropy alloy coatings of Fe20Co20Cr20Ni25 containing different atomic ratios of Al and Ti will be abbreviated as Al0Ti15, Al5Ti10, Al10Ti5, and Al15Ti0, respectively.

Table 1. Menu of Functions for Each Element

Elements	Features
Fe	It has the same main chemical composition as the 24CrNiMo matrix, thereby reducing differences in their thermophysical properties
Co	Prevent brittleness, enhance the wettability of the coating material and substrate, and improve friction and wear properties
Cr	It reacts with oxygen at high temperatures, enhancing the material's resistance to oxidation.
Ni	High thermal capacity reduces residual stress from machining and meets the requirement for increased thermal capacity on the brake disc surface
Al	This enhances wear resistance; Al_2O_3 forms at high temperatures, improving the material's resistance to high-temperature oxidation
Ti	A larger atomic radius can increase lattice distortion, thereby enhancing hardness and strength

Parameter validation of the thermodynamic phase stability and phase formation mechanisms in multi-component high-entropy alloys can effectively guide the design of high-entropy alloys. This paper calculates the phase stability, electronic properties, and elastic properties of the Fe20Co20Cr20Ni25AlxTi(15-x) high-entropy alloy system to ensure that the designed system is stable and capable of forming a disordered solid solution. It also elucidates the mechanisms by which the synergistic effects of Al and Ti in the high-entropy alloy system influence phase stability, electronic properties, and elastic properties.

Laser cladding is a computer-controlled process that uses a laser as a heat source to melt alloy powder and deposit it layer by layer onto the surface of a substrate. In this study, laser cladding was selected as the fabrication method to produce defect-free, dense coatings with high bond strength to the substrate and excellent performance.

This study investigates the effects of Al and Ti on the macrostructure of Fe20Co20Cr20Ni25AlxTi(15-x) high-entropy alloy coatings under optimal process parameters, the mechanisms governing their micro-shear properties, and their fundamental mechanical properties, including room-temperature tensile strength.

2. Materials and Methods

2.1. First-Principles calculation

This study uses Materials Studio 8.0 software (developed by Accelrys, Inc., USA) to perform DFT-based first-principles calculations. The Cambridge Sequential Total Energy Package (CASTEP) module is used to calculate the electronic and elastic properties, which utilizes the plane wave pseudopotential method and is a commonly used and accurate module for electronic calculations today. Crystal models built according to the SQS model approach were established on Ni with a single-phase FCC structure. The unoptimized crystal model of each high-entropy alloy was extended to a 1 × 1 × 5 supercell model containing 20 atoms, as shown in Fig. 1. Because of the different atomic properties of each element and different degrees of lattice distortion due to different atomic sizes, the random distribution of atoms does not minimize the formation energy, so structural stress relaxation is required for each high entropy alloy SQS model to calculate the most stable atomic composition before performing electronic and elastic property calculations. During the calculation, the interaction between electrons and ions is described using the mode-conserving pseudopotential (NCP). The electron exchange-correlation term is expressed in terms of the Perdew Burke Ernzerhof (PBE) density function in the Generalized Gradient Approximation (GGA). The plane wave truncation energy calculation accuracy is set to Ultra-fine to increase the calculation accuracy, at this time Ecut is 990 eV, other parameters are set by system default, each high entropy alloy model is divided into grids according to the Monkhorst-Pack method, and the k-point Brillouin zone sampling integral is set to 7×7×1. The geometry optimization was later performed using the Broyden Flecher Goldfarb Shanno (BFGS) mechanism to obtain the theoretically most stable structure, and the self-consistent calculations were performed using the Pulay density mixing method. The conditions for convergence of the self-consistent fields for the high-entropy alloys are total energy below 5.0E-6 eV/atom, Maximum force below 0.01 eV/Å, Maximum stress not more than 0.02 GPa and Maximum displacement less than 5.0E-4 Å, respectively. Geometric optimization was performed before the calculation of energy bands, density of states, and elastic properties for all models.

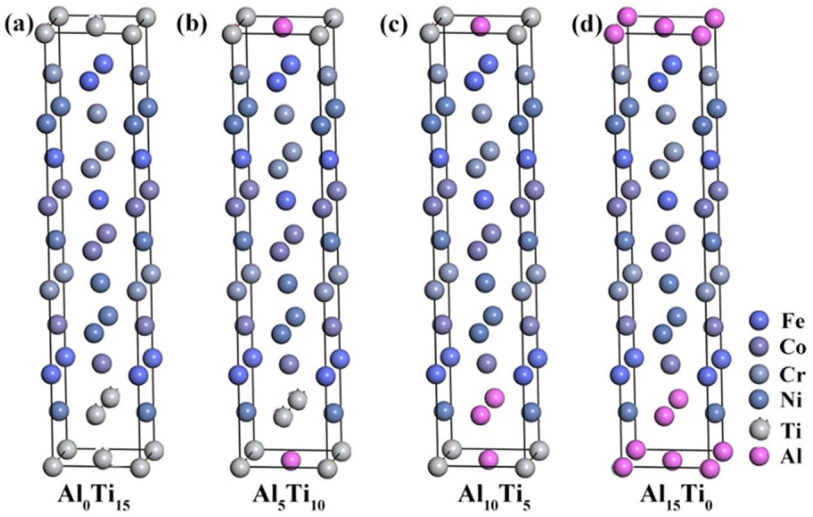

Figure 1. Constructed SQS model for high entropy alloys (a)Al0Ti15; (b)Al5Ti10; (c)Al10Ti5; (d)Al15Ti0

2.2. Sample preparation

The substrate material is 24CrNiMo cast steel, with dimensions of 200 mm × 100 mm × 8 mm. The metal powders used are pure Fe, Co, Cr, Ni, Al, and Ti powders, all with particle sizes ranging from 50 to 150 μm. An appropriate amount of the mixture was prepared using a ball-to-powder ratio of 10:1 and placed into two separate ball mills for grinding in a planetary ball mill for 8 hours. Prior to the laser cladding experiments, the prepared high-entropy alloy powder was dried for 2 hours in a vacuum oven maintained at a constant temperature of 100 °C. The mixing ratios are shown in Table 2.

Table 1. Elemental Composition of High-Entropy Alloy Powders (wt.%)

Sample	Fe	Co	Cr	Ni	Al	Ti
Al0Ti15	20.231	21.348	18.836	26.577	0	13.008
Al5Ti10	20.621	21.760	19.199	27.090	2.491	8.840
Al10Ti5	21.026	22.188	19.577	27.622	5.079	4.507
Al15Ti0	21.448	22.633	19.969	28.177	7.772	0

Laser cladding equipment primarily consists of a laser, a water-cooling circulation system, a shielding gas system, a powder feed system, a travel system, and a control system. The laser source used is an RFL-C6000 fiber laser with a power output of 6 kW, a wavelength of 1064 nm, and a spot diameter of 3 mm. A water-cooling circulation system ensures the laser operates normally without overheating during the cladding process. The powder feeding system consists of a DF-5000 synchronous turntable-type powder feeder and a three-point nozzle, allowing for adjustment of the powder feed rate and carrier gas flow (the carrier gas is 99.999% high-purity argon). The protective gas system supplies 99.999% high-purity argon coaxially with the laser. The motion mechanism provides three-axis, multi-directional movement with a precision of 0.01 mm.

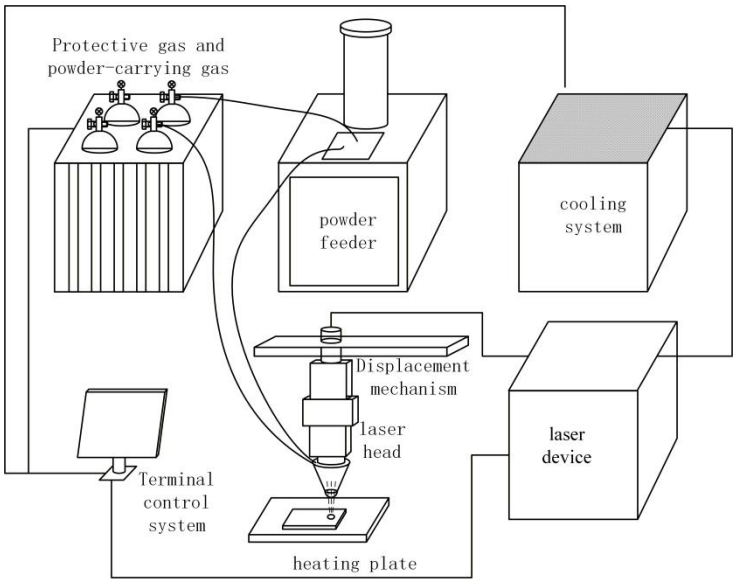

Figure 2. Laser Cladding System

2.3. Mechanical properties

2.3.1. Micro-shearing

In the experiment, a homemade miniature shear tester was used to measure shear strength and penetration rate. Shear strength is defined as the ratio of the maximum load to the initial cross-sectional area of the specimen, while penetration rate is the ratio of the area of the blade's penetration into the specimen's cross-section prior to fracture to the initial cross-sectional area. During the experiment, the shear rate was set at 1.8 mm/min, and a computer-integrated system was used to record the load and displacement. During the experiment, the shear rate was 1.8 mm/min, and a computer-integrated system was used to record the load and displacement. The sampling locations for the shear specimens are shown in Fig 3(a). The shear specimens measured 1.5 mm × 1.5 mm × 15 mm, with three sets of measurements taken from each of the three regions: the base material, the heat-affected zone, and the cladding layer. A schematic diagram of the micro-shear test is shown in Fig 3(b).

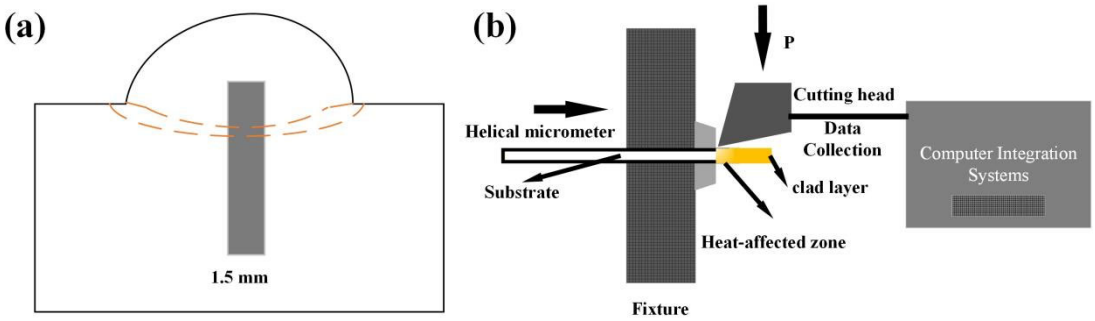

Figure 3. (a) Schematic of shear specimen preparation; (b) Schematic of a miniature shear test

2.3.2. Tensile Testing at Room Temperature

The tensile properties of four high-entropy alloys were tested at room temperature using a CMT5504-5105 series electronic universal testing machine, with a tensile strain rate of 0.5 mm/min. The tensile testing of the specimens was conducted in accordance with GB/T 228.1-2010, "Tensile Testing of Metallic Materials." To ensure the reliability of the data, three parallel specimens were tested for each group.

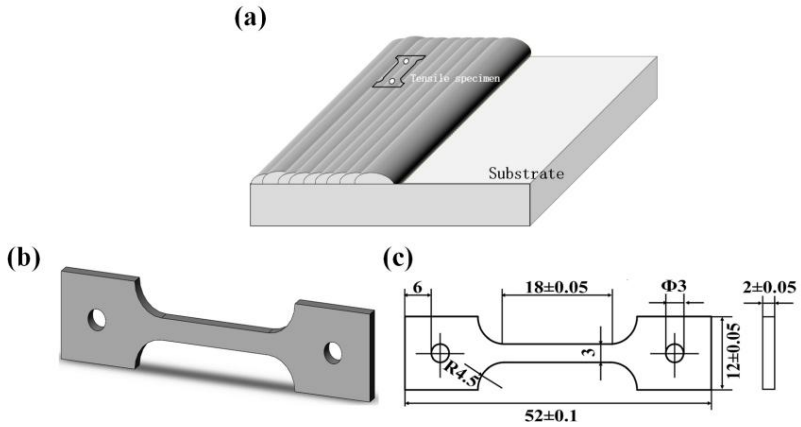

Figure 4. (a) Cross-sectional view; (b) 3D view of the tensile specimen; (c) Dimensions (mm)

3. Results

3.1. First-principles calculation results

3.1.1. Parameter calculation

ΔSmix, ΔHmix, δ, Ω(T), Δχ and VEC are calculated according to Formula (1)~ Formula (11) and Enthalpy of mixing between elements (shown in Table 3), and the calculated results of the phase stability parameters of the high entropy alloy are shown in Table 4.

Table 3. Enthalpy of mixing between elements

Binary mixing enthalpy (KJ/mol)	Fe	Co	Cr	Ni	Al	Ti
Fe	0	-1	-1	-2	-11	-17
Co		0	-4	0	-19	-28
Cr			0	-7	-10	-7
Ni				0	-22	-35
Al					0	-30
Ti						0

Table 4. Calculated results of phase stability parameters of Fe20Co20Cr20Ni25AlxTi(15-x) high entropy alloys

Sample	ΔSmix(J/K·mol)	ΔHmix(KJ/mol)	δ (%)	Ω(T)	$\Delta\chi$	VEC
Al0Ti15	13.28	-14.25	5.61	17.54	0.34	7.50
Al5Ti10	14.07	-13.72	5.44	18.80	0.35	7.45
Al10Ti5	14.07	-12.59	5.26	19.93	0.33	7.40
Al15Ti0	13.28	-10.86	5.07	21.19	0.25	7.35

Mixed entropy:

$$\Delta S_{mix} = -R\sum_{i=1}^{n} c_i \ln c_i \quad (1)$$

Mixing enthalpy:

$$\Delta H_{mix} = \sum_{n}^{i=1, i\neq j} (4\Delta H_{ij}^{mix} c_i c_j) \quad (2)$$

Gibbs Free Energy:

$$\Delta G_{mix} = \Delta H_{mix} - T\Delta S_{mix} \quad (3)$$

Atomic size radius difference:

$$\delta = \sqrt{\sum_{i=1}^{n} c_i (1 - \frac{r_i}{\bar{r}})} \quad (4)$$

$$\bar{r} = \sqrt{\sum_{i=1,\, j=1}^{n} c_i r_i} \quad (5)$$

Electronegativity difference:

$$\Delta\chi = \sqrt{\sum_{i=1}^{n} c_i \left|\chi_1 - \bar{\chi}^2\right|} \quad (6)$$

$$\bar{\chi} = \sum_{i=1}^{nn} c_i \chi_i \quad (7)$$

Entropy to enthalpy ratio:

$$\Omega = \frac{T_m \Delta S_{mix}}{\left|\Delta H_{mix}\right|} \quad (8)$$

$$T_m = \sum_{i=1}^{n} c_i \left|T_{mi}\right| \quad (9)$$

Atomic size mismatch degree:

$$r = \left(1 - \sqrt{\frac{(r_s + \bar{r})^2 - \bar{r}^2}{(r_s + \bar{r})^2}}\right) / \left(1 - \sqrt{\frac{(r_1 + \bar{r})^2 - \bar{r}^2}{(r_1 + \bar{r})^2}}\right) \quad (10)$$

Valence electron concentration:

$$VEC = \sum_{i=1}^{n} c_i (VEC)_i \quad (11)$$

According to the proposed empirical criterion of whether the high-entropy alloys can form solid solutions, of high-entropy alloys between 5.00 and 5.65, all less than 6.5% and all satisfy Ω(T) ≥ 1.1, can form disordered solid solutions. The VEC of high entropy alloys is between 6.8 and 8.5, which indicates all belong to the mixed-phase structure of FCC and BCC according to the VEC The ΔHmix is in the range of -15 and 5 kJ/mol and the ΔSmix is in the range of 12 and 17.5 J/mol·k, which is large enough to facilitate the formation of a stable simple solid solution. Hence, the formation of a simple solid solution of Fe20Co20Cr20Ni25AlxTi(15-x) high-entropy alloy can be demonstrated.

3.1.2. Electronic properties

The energy band structure and density of states (DOS) can predict the properties of materials and thus investigate the structural properties of solids, and the calculated results of the energy band structure and density of states in Fig. 5. The energy band structure and density of states near the Fermi energy level (0 eV) are closely related to the properties of materials. The closer the distance between the energy bands in the energy band structure, the stronger the electrical interaction between the atoms and the stronger the bond strength of the alloy system. The valence and conduction bands near the Fermi energy level are heavily hybridized, and all structures have positive values of density of states at 0 eV, indicating that all high-entropy alloys have metallic properties. Al0Ti15, Al5Ti10, and Al10Ti5 have similar energy band structures, which means that these three alloys have similar structures and properties with strong stability. The valence band near the Fermi energy level is mainly contributed by d-orbital electrons, followed by p- and s-orbital electrons, while the conduction band is mainly formed by the hybridization of p- and s-orbital electrons. The absence of peaks and troughs in the density of states in the high-energy region of the conduction band of the high-entropy alloy and the tighter energy band indicates that the interactions between the metal atoms of the Fe20Co20Cr20Ni25AlxTi(15-x) high-entropy alloy are stronger.

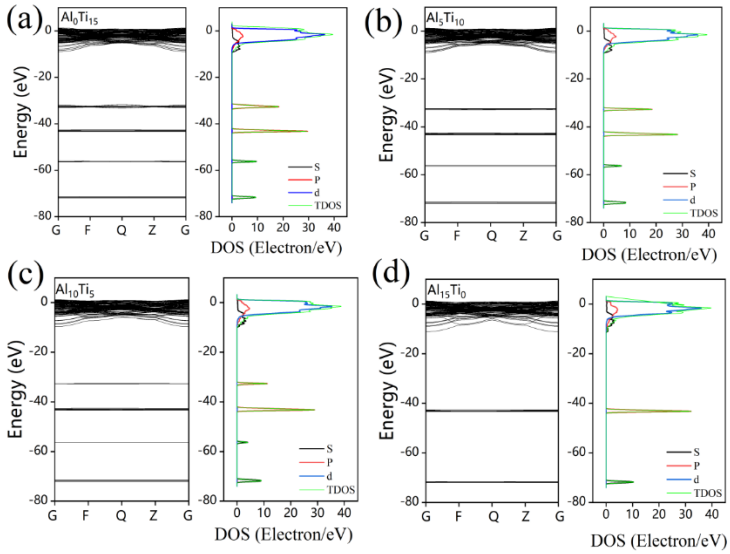

Figure 5. The band structures and density of states for the SQS model of high entropy alloys.

3.1.3. Elastic properties

The mechanical stability of an alloy can be judged by the elastic constant. The elastic constants of crystals reflect the macroscopic mechanical properties of material under normal temperature and pressure or static load, reflect the form of the material's response to applied stress or strain, and also reflect the microscopic characteristics of the electron bonding features within the material. According to elasticity theory, in cubic crystal systems, there are usually three independent elastic constants: C11, C12 and C44. The subsequent mechanical property calculations are performed by calculating the average of the resulting elastic constants to reduce the effect of low symmetry and large size of the SQS supercell model on the accuracy of the calculations [6], as follows:

$$C_{11} = \frac{C_{11}^{'} + C_{22}^{'} + C_{33}^{'}}{3} \tag{12}$$

$$C_{12} = \frac{C_{12}^{'} + C_{23}^{'} + C_{13}^{'}}{3} \tag{13}$$

$$C_{44} = \frac{C_{44}^{'} + C_{55}^{'} + C_{66}^{'}}{3} \tag{14}$$

For the Fe20Co20Cr20Ni25AlxTi(15-x) system alloy based on the FCC structure studied in this paper, the mechanical stability criterion in the ground state (0 K, 0 GPa) is [7]:

$$C_{ij} > 0; C_{11} + C_{22} > 2C_{12} \tag{15}$$

$$C_{11} + C_{33} > 2C_{13}; C_{22} + C_{33} > 2C_{23} \tag{16}$$

$$C_{11} + C_{22} + C_{33} + 2C_{12} + 2C_{13} + 2C_{23} > 0 \tag{17}$$

Generally, Cauchy pressure is used to evaluate the ductility of high-entropy alloys [8]. If the Cauchy pressure is positive, the alloy forms metallic bonds and is ductile, and the positive value has a positive correlation with the ductility; if it is negative, the alloy forms covalent bonds and becomes brittle, and the larger the negative value, the more brittle the alloy is. The average elastic constants, Cauchy pressure and mechanical stability of the high-entropy alloys are calculated in Table 5.

All C11-C12 of the high entropy alloys have positive values, so the alloys in this system can form intermetallic and have good ductility in the ground state. According to the mechanical stability criterion, Fe20Co20Cr20Ni25AlxTi(15-x) high-entropy alloy has larger, and, which indicates better mechanical stability, and Al5Ti10 has the largest of these parameters, indicating that this high-entropy alloy has better mechanical stability compared with other high-entropy alloys.

Table 5. Calculated average elastic constants, Corsi pressure and mechanical stability of Fe20Co20Cr20Ni25AlxTi(15-x) high entropy alloy

Sample	Elastics C_{ij} (GPa)					
	C_{11}	C_{22}	C_{44}	$C_{12}-C_{44}$	$C_{11}-C_{12}$	$C_{11}+2C_{12}$
Al0Ti15	376.52	236.90	157.26	79.64	139.63	850.32
Al5Ti10	367.80	218.74	172.50	46.24	149.05	805.28
Al10Ti5	335.45	194.21	161.24	32.96	141.24	723.86
Al15Ti0	345.18	203.12	172.34	30.78	142.06	751.42

The Voigt-Reuss-Hill (VRH) method was used to study the mechanical properties of high-entropy alloy polycrystals.

Bulk modulus is a physical quantity that characterizes the resistance of a crystal to bulk deformation under external pressure. Shear modulus is a physical quantity that characterizes the resistance of a crystal to reversible deformation under shear stress and usually reflects the hardness of the alloy. Young's modulus is the physical quantity that characterizes the resistance of a crystal to compression or tension within the elastic limit and is expressed as the stiffness of an alloy [9]. The material shear modulus, Young's modulus, and Poisson's ratio directly affect the inherent hardness and plasticity of the material [10].

The polycrystalline bulk modulus B can be approximated by the following equation:

Voigt approximation:

$$C_{11}+C_{22}+C_{33}+2C_{12}+2C_{13}+2C_{23}>0 \quad (18)$$

Reuss approximation:

$$C_{11}+C_{22}+C_{33}+2C_{12}+2C_{13}+2C_{23}>0 \quad (19)$$

Hill approximation:

$$C_{11}+C_{22}+C_{33}+2C_{12}+2C_{13}+2C_{23}>0 \quad (20)$$

The shear modulus can be approximated by the following equation:

Voigt approximation:

$$C_{11}+C_{22}+C_{33}+2C_{12}+2C_{13}+2C_{23}>0 \quad (21)$$

Reuss approximation:

$$C_{11}+C_{22}+C_{33}+2C_{12}+2C_{13}+2C_{23}>0 \quad (22)$$

Hill approximation:

$$C_{11}+C_{22}+C_{33}+2C_{12}+2C_{13}+2C_{23}>0 \quad (23)$$

Young's modulus and Poisson's ratio can be calculated by the following equations:

$$C_{11}+C_{22}+C_{33}+2C_{12}+2C_{13}+2C_{23}>0 \quad (24)$$

$$C_{11}+C_{22}+C_{33}+2C_{12}+2C_{13}+2C_{23}>0 \quad (25)$$

Table 6 shows the simulation results of the average elastic modulus and Poisson's ratio of Fe20Co20Cr20Ni25AlxTi(15-x) high entropy alloy. The plasticity of high entropy alloys can be predicted from the ratio of shear modulus to bulk modulus. The Fe20Co20Cr20Ni25AlxTi(15-x) alloys are less than 0.57 and around 1/3, indicating that all four compositions of the high entropy alloys are ductile. When the Al content increases and the Ti element content decreases, it increases and decreases accordingly. The Al5Ti10 alloy has the largest and predicts the largest strength and hardness.

Table 6. Simulation results of average elastic modulus and Poisson's ratio of Fe20Co20Cr20Ni25AlxTi(15-x) high entropy alloy

Sample	*B*	*G*	*E*	*ν*	*G*/*B*
Al0Ti15	283.23	113.49	300.35	0.32	0.40
Al5Ti10	273.05	120.42	314.96	0.31	0.44
Al10Ti5	245.05	113.22	294.33	0.30	0.46
Al15Ti0	250.35	120.62	311.79	0.29	0.48

3.2. Macroscopic morphology of high-entropy alloy coatings

The macroscopic surface morphology of the cladding layers is shown in Fig 6. The surfaces of the Al0Ti15, Al0Ti15, Al0Ti15, and Al0Ti15 cladding layers appear pale blue, pale yellow, bright yellow, and silvery white, respectively; the metallic color of the surface is related to the metal composition. The width and height of the Fe20Co20Cr20Ni25AlxTi(15-x) high-entropy alloy coating remained stable, and the coating surface showed no obvious defects such as pores or cracks, indicating that the elemental composition of the high-entropy alloy and the process optimization designed in this study to meet performance requirements are well-matched. The coating thickness of the Al10Ti5 and Al15Ti0 coatings exhibits slight fluctuations. This is due to the fact that, during the laser cladding process, a higher concentration of aluminum leads to more severe burn-through or spatter.

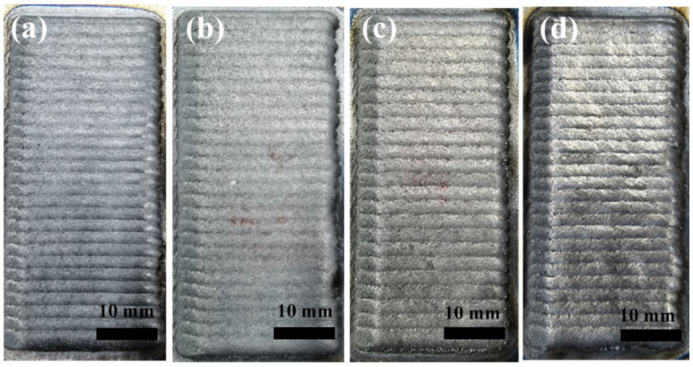

Figure 6. Macroscopic surface morphology of high-entropy alloy coatings (a)Al0Ti15; (b)Al5Ti10; (c)Al10Ti5; (d)Al15Ti0

Fig 7 shows the macroscopic morphology of a single cross-section of the high-entropy alloy coating prepared under optimal parameters. The cross-section of the high-entropy alloy cladding layer, prepared using process parameters optimized through orthogonal experiments, exhibits no obvious defects and demonstrates good formation quality. The white dashed line indicates the boundary between the heat-affected zone and the substrate.

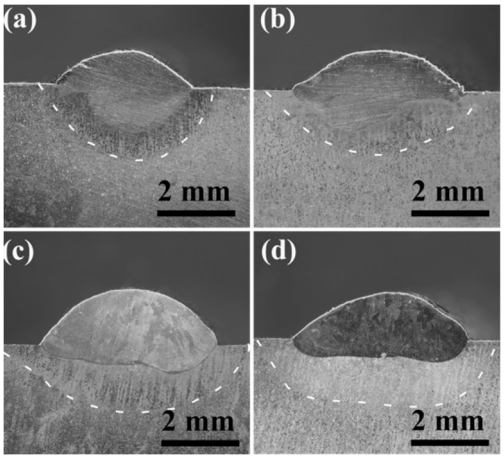

Figure 7. Macroscopic cross-sectional morphology of a single-layer coating on a high-entropy alloy (a)Al0Ti15; (b)Al5Ti10; (c)Al10Ti5; (d)Al15Ti0

3.3. Mechanical properties

3.3.1. Micro-shear properties

Since the cross-sectional dimensions of each sample vary during machining and fine grinding, incorporating shear strength allows for a more accurate characterization of the shear resistance of each micro-region within the cladding layer. The shear penetration ratio α characterizes a material's capacity for plastic deformation. Regardless of composition, the shear strength of high-entropy alloys decreases in the following order: cladding layer, heat-affected zone, and base metal. In Fig 8, the shear strength of the Al5Ti10 coating reached a maximum of 714.8 MPa, which is 24.92% higher than that of the base material. The shear strength of the cladding layers for all compositions exceeded 635 MPa, while that of the heat-affected zones was around 550 MPa. The shear strength of the base material was approximately 520 MPa, indicating a high bond strength between the substrate and the coating.

The indentation rates of the Al5Ti10, Al10Ti5, and Al15Ti0 cladding layers are all above 25%, with little difference among them. The indentation rate of the Al0Ti15 cladding layer did not reach 20%. This is attributed to the fine, narrow columnar grains and the relatively high number of Ti-rich white particles characteristic of high-entropy alloys, which give Al0Ti15 high hardness and strength but poor ductility. Overall, the indentation rates of the high-entropy alloy cladding layers for all four compositions were lower than those of the base material, while their shear strengths were all higher than those of the base material.

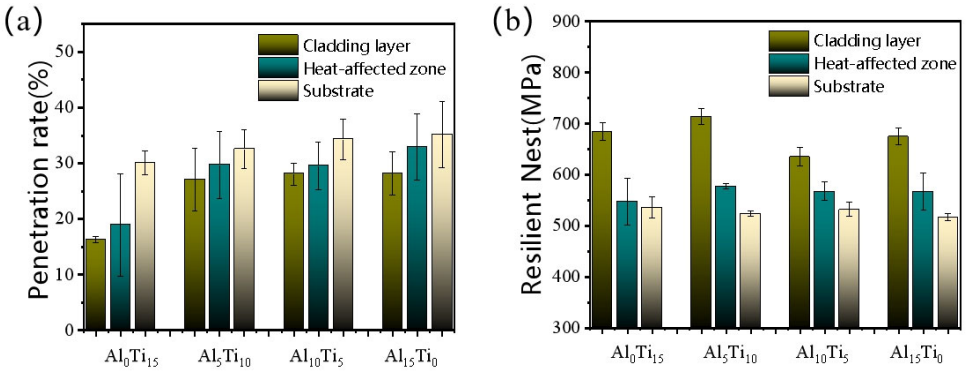

Figure 8. Shear properties of the cladding layer: (a) shear strength; (b) indentation rate

Fig 9 dims the macroscopic and microscopic fracture surfaces of the Al0Ti15 high-entropy alloy coating. The microscopic fracture surface of the substrate exhibits large, shallow, equiaxed and elongated dimples, surrounded by numerous densely packed small dimples. The fracture surface in the heat-affected zone is relatively flat, displaying two characteristic morphologies: cleavage steps and small dimples. The fracture surface of the cladding layer exhibits distinct cracks and intergranular fracture, indicating its brittle nature; therefore, the shear fracture mode of the Al0Ti15 cladding layer is classified as brittle fracture. Upon examination of the substrate fracture surface, it was found that the fracture characteristics were essentially identical, and the fracture mode was ductile fracture; thus, it will not be repeated in the subsequent fracture morphology Figs.

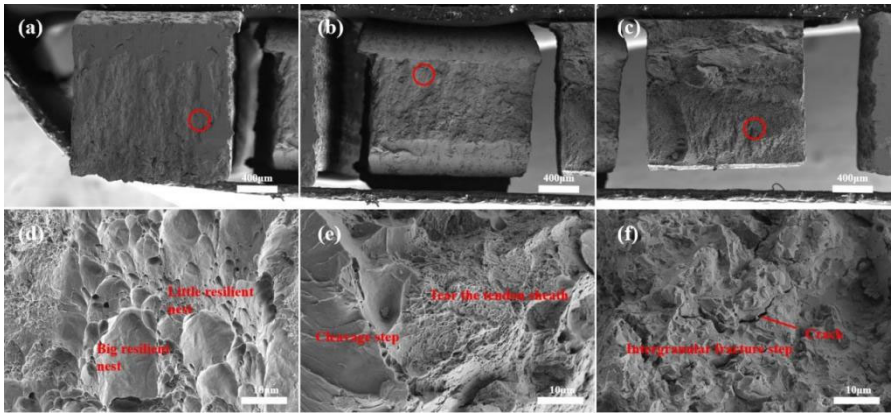

Figure 9. Macroscopic and microscopic fracture surfaces of Al0Ti15: (a) base metal; (b) heat-affected zone; (c) cladding layer; (d) magnified view of the area circled in white in (a); (e) magnified view of the area circled in white in (b); (f) magnified view of the area circled in white in (c)

Fig 10 shows the macroscopic and microscopic fracture surfaces of the Al5Ti10 high-entropy alloy coating. The fracture surface is smooth and exhibits a river-like pattern, which results from the intersection of multiple steps during cleavage fracture propagation. The heat-affected zone exhibits two types of ductile pits of varying sizes, while the fracture surface of the cladding layer shows distinct shear-induced ductile pits, indicating ductile fracture.

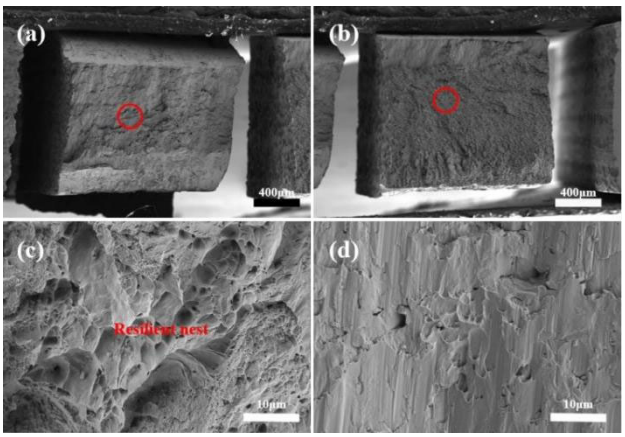

Figure 10. Macroscopic and microscopic morphologies of the Al5Ti10 fracture surface: (a) heat-affected zone; (b) cladding layer; (c) magnified view of the area circled in white in (a); (d) magnified view of the area circled in white in (b)

Fig 11 shows the macroscopic and microscopic fracture surfaces of the Al10Ti5 high-entropy alloy coating. The fracture surface of the heat-affected zone is uneven, whereas that of the cladding layer is smooth. A smooth fracture surface typically results from slip along a specific crystal plane under stress, forming a [11] slip plane. In the fracture surface of the cladding layer, microvoids elongated along the shear direction under shear stress form shear-induced pits, indicating that the fracture mode of the cladding layer's shear fracture is ductile fracture.

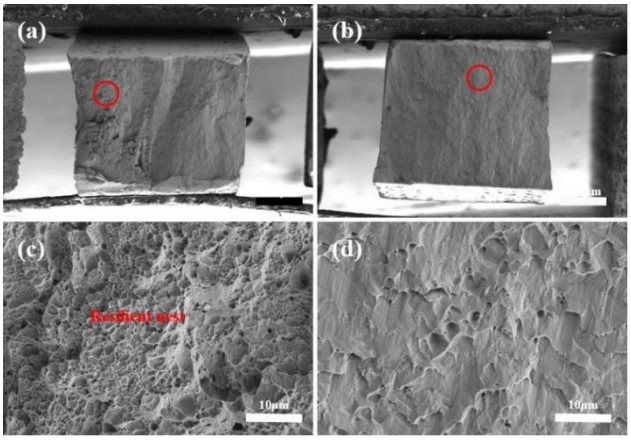

Figure 11. Macroscopic and microscopic morphologies of the Al10Ti5 fracture surface: (a) heat-affected zone; (b) cladding layer; (c) magnified view of the area circled in white in (a); (d) magnified view of the area circled in white in (b)

Fig 12 shows the macroscopic and microscopic fracture surfaces of the Al15Ti0 high-entropy alloy coating. The fracture surface in the heat-affected zone is uneven, and the microscopic fracture surface exhibits ductile pits. The fracture surface of the cladding layer is smooth, with no obvious irregularities. The microscopic features of the cladding layer's fracture surface consist of shear ductile pits, indicating that the fracture mode of the cladding layer is ductile fracture.

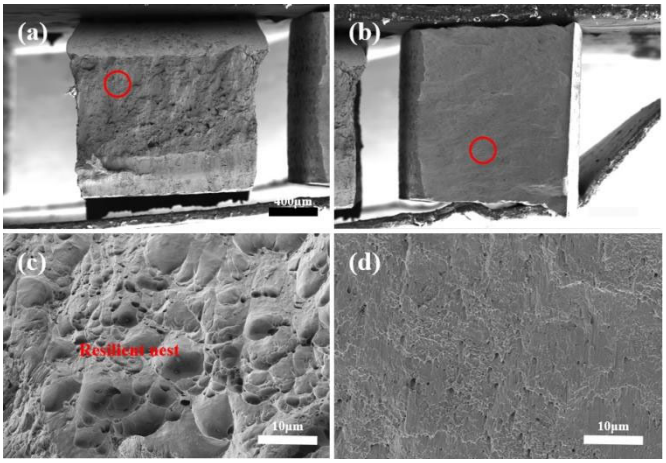

Figure 12. Macroscopic and microscopic morphologies of the fracture surface of Al15Ti0: (a) heat-affected zone; (b) cladding layer; (c) magnified view of the area circled in white in (a); (d) magnified view of the area circled in white in (b)

3.3.2. Tensile Properties at Room Temperature

Fig 13 shows the tensile stress-strain curves for tensile specimens of the Fe20Co20Cr20Ni25AlxTi(1-x) high-entropy alloy coating under optimal parameters. The plasticity of the Al10Ti5 and Al15Ti0 specimens has improved relative to the base material, but their yield strength has decreased significantly. In tensile tests, elongation (A) is commonly used as an indicator of a material's ductility. Table 7 presents the tensile properties of the base material and the high-entropy alloys. The yield strength and tensile strength of the high-entropy alloy coatings are both lower than those of the base material; the Al5Ti10 cladding layer, which exhibits the highest tensile strength, has a tensile strength that is 8% lower than that of the base material.

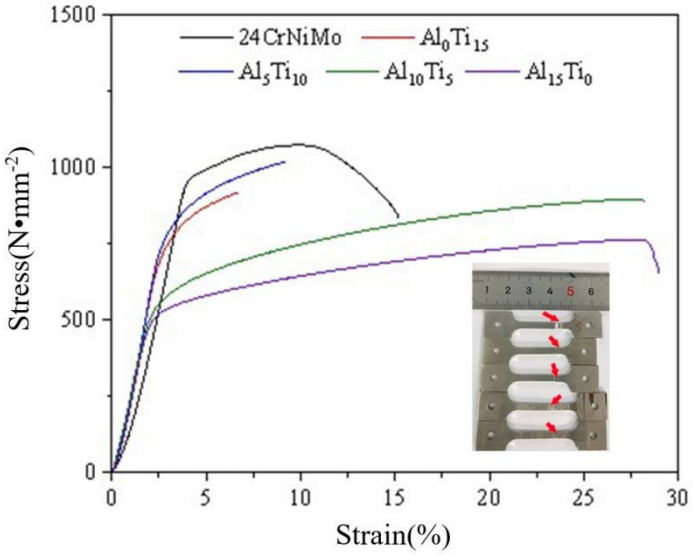

Figure 13. Stress-strain curve

As shown in Table 7, as the Al content increases, the Ti content decreases; the yield strength and tensile strength first increase and then decrease, while the elongation increases accordingly, which is consistent with the results reported by Ding [12]. Al5Ti10 exhibits the highest yield strength and tensile strength. The yield strength of Al5Ti10 is 6.67%, 32.94%, and 34.77% higher than that of Al0Ti15, Al10Ti5, and Al15Ti0, respectively. The elongation of Al10Ti5 and Al15Ti0 exceeds 20% and differs only slightly, indicating that when the aluminum content exceeds 10%, there is little difference in the strength and ductility of the alloy. Research has shown that, without altering the composition, post-heat treatment can be used to improve the room-temperature tensile properties of high-entropy alloys[13].

Table 7. Tensile Properties of the Matrix and High-Entropy Alloys

Materials	$\sigma_{0.2}$ (MPa)	σ_b (MPa)	A(%)
24CrNiMo	998.97±57.14	1104.93±55.02	12.93±2.45
Al0Ti15	714.06±6.22	917.12±10.18	4.63±0.67
Al5Ti10	765.35±5.56	1015.81±14.22	8.87±1.48
Al10Ti5	513.75±6.22	880.82±16.93	24.29±0.36
Al15Ti0	498.95±7.37	782.28±25.78	23.04±4.83

The macroscopic fracture surfaces of the tensile tests are shown in Fig 14. The base metal exhibits significant necking and a large number of tear ridges. The fracture surfaces of the high-entropy alloy coatings show no obvious necking, and the plastic deformation is minimal. The fracture surfaces of Al0Ti15 and Al10Ti5 are uneven, while that of Al5Ti10 is smooth; the slip direction forms a 45° angle with the base, suggesting that specific crystal planes slip under shear stress.

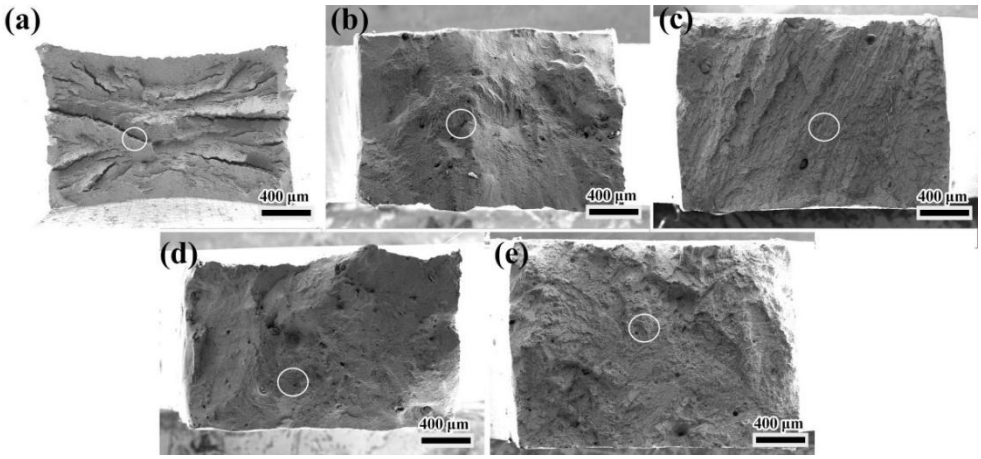

Figure 14. Macroscopic morphology of the tensile fracture surface (a)24CrNiMo; (b)Al0Ti15; (c)Al5Ti10; (d)Al10Ti5; (e)Al15Ti0

Fig 15 shows an enlarged view of the microstructure of the tensile fracture surface in the white area of Fig 14. The fracture surfaces of the Al0Ti15, Al5Ti10, and Al10Ti5 coatings all exhibit tearing ridges, and the orientation of these ridges is consistent with the direction of dendrite growth, which may be related to the dendritic microstructure. Tear ridges are a typical feature of ductility and result from plastic deformation. In addition, there are some ductility pits, and their distribution bears similarities to that of dendrites. The internal notch of the Al10Ti5-coated tear ridge is free of impurities and consists of clusters of micro-pores. Under tensile stress, the original notch elongates and, as the degree of plastic deformation increases, continues to expand and interconnect, ultimately leading to fracture. The fracture surface of Al15Ti0 exhibits tear-type ductile pits, which are distributed across the lamellar fracture surface, indicating ductile fracture.

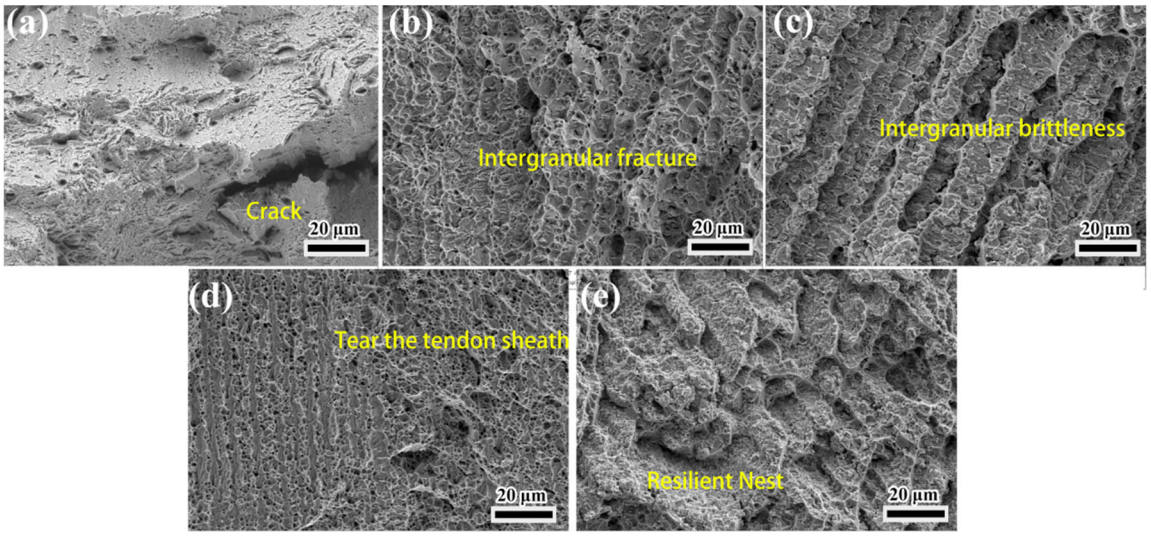

Figure 15. Microstructure of the tensile fracture surface (a)24CrNiMo; (b)Al0Ti15; (c)Al5Ti10; (d)Al10Ti5; (e)Al15Ti0

4. Conclusion

A macroscopic morphological analysis was conducted on Fe20Co20Cr20Ni25AlxTi(15-x) high-entropy alloy coatings prepared by laser cladding. The shear properties and room-temperature tensile properties of the high-entropy alloy coatings were tested, and their mechanisms of action were investigated. The following conclusions were drawn:

(1) Using laser cladding, prepare a high-entropy alloy coating with no obvious surface defects and good metallurgical bonding to the substrate under optimal process parameters.

(2) The shear strength decreases in the following order: cladding layer, heat-affected zone, and base metal. The shear strength of Al5Ti10 exceeds 700 MPa, which is 24.92% higher than that of the base metal, and its indentation rate is over 25%. Al0Ti15, Al5Ti10, Al10Ti5, and Al15Ti0 had tensile strengths of 1104.93 ± 55.02 MPa, 917.12 ± 10.18 MPa, 1015.81 ± 14.22 MPa, 880.82 ± 16.93 MPa, and 782.28 ± 25.78 MPa, respectively. As the aluminum content increases, both shear and tensile fracture modes at room temperature transition from brittle fracture to ductile fracture.

Acknowledgements

This research received no external funding.

References

[1] Guo, S., Ng, C., Lu, J., et al. (2011). Effect of valence electron concentration on stability of fcc or bcc phase in high entropy alloys. *Journal of Applied Physics*, *109*(10), 213. https://doi.org/10.1063/1.3587228

[2] Z, C. L., & S, C. Y. (2020). Inverse Hall-Petch relationship of high-entropy alloy by atomistic simulation. *Materials Letters*, *274*. https://doi.org/10.1016/j.matlet.2020.128024

[3] Zhou, J. L., & Kong, D. J. (2020). Effects of Al and Ti additions on corrosive–wear and electrochemical behaviors of laser cladded FeSiB coatings. *Optics & Laser Technology*, *124*, 105958.

[4] Ding, L., Hu, S. S., Quan, X. M., et al. (2018). Effect of Ti on the microstructure evolution and wear behavior of VN alloy/Co-based composite coatings by laser cladding. *Journal of Materials Processing Technology*, *252*, 711-719.

[5] Yang, Y. C., Liu, C. X., Lin, C. Y., et al. (2021). The effect of local atomic configuration in high-entropy alloys on the dislocation behaviors and mechanical properties. *Materials Science and Engineering: A*, *815*, 141253.

[6] Wang, J., Chen, Y., Zhang, Y., Dai, W., Xu, Q., Li, W., & Liu, Y. (2021). Corrosion and slurry erosion wear performances of coaxial direct laser deposited CoCrFeNiCu1-xMox high-entropy coatings by modulating the second-phase precipitation. *Materials & Design*, *212*, 110277. https://doi.org/10.1016/j.matdes.2021.110277

[7] Nye, J. F. (1985). *Physical properties of crystals*. Oxford University Press.

[8] Chang, C., & Zhang, H. (2022). First-principles calculations to investigate elastic and thermodynamic properties of FeAlNixCrMn quinternary alloys. *Journal of Materials Research and Technology*, *18*, 1322–1332. https://doi.org/10.1016/j.jmrt.2022.03.046

[9] Yin, B., & Curtin, W. A. (2019). First-principles-based prediction of yield strength in the RhIrPdPtNiCu high-entropy alloy. *npj Computational Materials*, *5*. https://doi.org/10.1038/s41524-019-0151-x

[10] Nakamura, K., Ohnuma, T., & Ogata, T. (2011). First-principles study of structure, vacancy formation, and strength of bcc Fe/V4C3 interface. *Journal of Materials Science*, *46*(12), 4206-4215.

[11] Shumpert, R. H., Jaspreet, P., & Barazanchy, D. (2024). Thermo-folding thermoplastic composite laminates. *AIAA SCITECH 2024 Forum*. https://doi.org/10.2514/6.2024-1469

[12] Ding, Z. Y., Cao, B. X., Luan, J. H., et al. (2021). Synergistic effects of Al and Ti on the oxidation behaviour and mechanical properties of L12-strengthened FeCoCrNi high-entropy alloys. *Corrosion Science*, *184*, 109365.

[13] Yin, Z. H., Gao, N., Fan, S., et al. (2022). Microstructure evolution and tensile property of a CuMnFeCoNi high-entropy alloy during thermomechanical treatment. *Metallurgical and Materials Transactions A*, *53*(12), 4393-4403.